

WFC3/UVIS-Cycle17: CTE External Monitoring - NGC6791

V. Kozhurina-Platais, R. Gilliland, & S. Baggett

February 3, 2011

Abstract

We present preliminary results of the Charge Transfer Efficiency (CTE) evaluation based on external calibration observations from the new instrument Wide Field Camera 3 (WFC3), a fourth - generation imaging instrument which was installed in HST during Servicing Mission 4 in May 2009. Observations of the rich open cluster NGC6791 have been used to provide an initial assessment of the WFC3/UVIS CTE and its dependence with time. The observations with low-sky background ($\sim 0.1\text{--}1.0\ e^-$) for the flux range 500 to 2000 e^- exhibit a clear trend with Charge Transfer Inefficiency increasing from 2% in October 2009 to 7% in the fall of 2010. The CTE degradation will continue to be monitored with both internal and external observations. Additional observations of NGC6791 and 47Tuc (CAL-12379, PI K. Noeske) planned for the fall of 2010 and spring of 2011, will be used to develop formal photometric and astrometric corrections for WFC3 science data.

1. Introduction

It is a well-known fact that there is a significant loss of Charge Transfer Efficiency (CTE) for all HST CCDs in the environment of space: WFPC2 (Whitmore *et al.* 1999, Dolphin 2000), STIS (Gilliland *et al.* 1999; Goudfrooij & Kimble 2003; Goudfrooij *et al.* 2007) and ACS (Riess 2003; Mutchler & Siriani 2005). CTE degradation in the CCD detectors is due to damage of the silicon lattice by cosmic rays. The CTE loss affects the precision of stellar photometry and astrometry on many HST science programs. An analysis

¹Copyright © 2003 The Association of Universities for Research in Astronomy, Inc. All Rights Reserved.

of CTE in ACS images by Riess & Mack (2004) provided an algorithm to correct the CTE-induced photometric losses in aperture photometry as a function of object position on WFC CCD chips, flux, sky background, observing epoch, and aperture size. This algorithm was derived from so-called drizzled (**_drz.fits*) images, i.e., ACS images corrected for geometric distortion by the Multidrizzle software (Koekemoer *et al.* 2002) that is currently installed in the ACS on-the-fly calibration (OTFR) pipeline. An independent measure of CTE-induced photometric losses in drizzled ACS images, along with photometric correction formula for both HRC and WFC were presented by Chiaberge *et al.* (2006) and Chiaberge *et al.* (2009).

Based on an *effective* PSF-fitting analysis of long and short exposures from ACS/WFC flat-fielded images (**_flt.fits*), Kozhurina-Platais *et al.* (2007, 2008) developed a differential correction for CTE-induced flux loss and CTE-induced centroid shifts. The CTE correction as described by their equations (4) & (7) is parametrized in terms of two variables only: the location of the source on the CCD chips (i.e., the WFC1 and WFC2 chips) and the instrumental magnitudes of sources, though in general, the correction for CTE loss depends on the sky background level as well. Recently, Anderson & Bedin (2010) developed a pixel-based correction for CTE induced flux loss and centroid shift in ACS/WFC (**_flt.fits*) images, which is now implemented into the HST CDBS pipeline.

In this paper we report the first CTE evaluation based on external calibration observations from the *Wide Field Camera 3* (WFC3). Observations of the rich open cluster NGC6791 began soon after the Servicing Mission 4 in October 2009 and continue through the first year of WFC3 (CAL-11924, PI Kozhurina-Platais). These early observations have been used to provide a preliminary assessment of the WFC3/UVIS CTE and its time dependence. Additional observations of NGC6791 and 47Tuc, planned for the fall of 2010 and spring of 2011, will be used to develop formal photometric and astrometric corrections for WFC3 science data.

2. Observations

Historically, the WFPC2 and ACS/WFC/HRC external CTE monitoring programs used globular clusters such as Omega Cen or 47 Tuc, which are rich stellar fields to ensure good statistics. However, with such a high density of stars, many pixels in a given column of the detector are exposed to starlight prior to the charge transfer, potentially serving as a *preflash* (filling traps) and mitigating some of the CTI (Charge Transfer Inefficiency). In order to avoid this effect a sparse stellar field was used as a target for the WFC3/UVIS CTE monitoring. Observations of the rich open cluster NGC6791 with WFC3 should avoid any possible *self preflash* and thus may provide a more accurate measurement of the CTE losses. The analysis of NGC6791 images from a 30-sec ACS/WFC observations show that there are ~ 1000 stars with fluxes of $\gtrsim 1000$ counts in the ACS/WFC FOV which is similar to

the WFC3 UVIS field of view (FOV). Also, NGC6791 has an ecliptic latitude of 59 degrees, increasing its visibility to HST and can be observed year round. NGC 6791 was chosen to test the hypothesis that a sparser stellar field will give a more accurate determination of CTE-induced losses. The open cluster NGC6791 was observed at $\alpha=19^{\text{h}}20^{\text{m}}53^{\text{s}}.97$ and $\delta=37^{\circ}48'09''.60$ during the Cycle 17 calibration program (CAL-11924, PI Kozhurina-Plarais) in three different epochs: October 2009, March 2010 and September 2010. Each epoch (visit) consists of two orbits and three pointings and a total of 12 exposures. During each visit, observations are taken through the F606W and F502N filters with 3 pointings of half-FOV size dithers in both X and Y directions. The large dither of 2051 pixels in the Y direction (or $80''$) allows for overlap of the UVIS1 CCD chip with the UVIS2 CCD chip for characterization of the parallel CTE induced losses. The large dither of 2051 pixels in the X direction (or $81''$) allowed for overlap half of the UVIS1 CCD chip with half of the UVIS2 CCD chip for characterization of the serial CTE induced losses. Each pointing consists of one short and one long exposure in each filter to ensure that the sky background is in the range between 0 to 50 e^- per pixel. Appendix A contains Table 1 with all observations of NGC6791.

3. Reduction and Analysis

3.1. WFC3/UVIS Charge-Transfer Efficiency

Before describing the data reduction techniques, we outline here the WFC3 CCD detector format and its structure as they relate to CTE measurements. The WFC3/UVIS CCDs are large-format devices, similar to ACS/WFC, and thus require a significant number of charge-shifting steps during readout compared to smaller devices such as the STIS and WFPC2 CCDs. As a result, effects due to radiation-induced CTI (Charge Transfer Inefficiency) will be encountered earlier than for the small-format detectors. As described in the WFC3 Instrument Handbook for Cycle 18 (Dressel *et al.*, 2010), each of the UVIS CCD detectors has 4096×2051 pixels. Both CCD chips have 25 extra columns on each side, which form the serial physical overscan regions. Each CCD chip also has 60 virtual serial overscan pixels in the center of each row. Next to the inter-chip gap there are 19 rows of parallel overscan for each CCD chip. Figure 1 shows the format of a raw image obtained with full-chip four-amplifier readout.

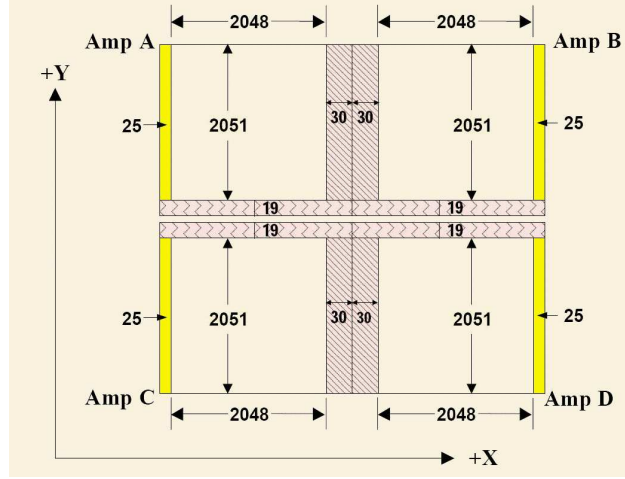


Fig. 1.— Schematic illustration of the standard WFC3 UVIS image from Figure 6.14 of the WFC3 Instrument handbook (Dressel *et al.* 2010). The 2051×2048 sections represent the CCD image area (science pixels). The bright yellow color shows serial physical overscan in X and the pink hatched areas indicates serial virtual and parallel in Y virtual overscan. The UVIS1 CCD chip is at the top and the UVIS2 CCD chip at the bottom.

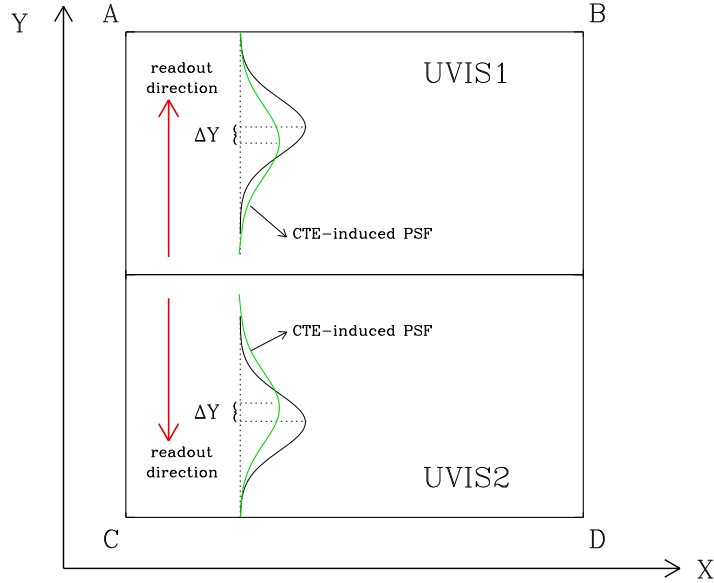


Fig. 2.— Schematic illustration of CTE loss in the two WFC3 UVIS chips. Red arrows show the parallel readout direction for the UVIS1 and UVIS2 chips. Solid black lines indicate schematic PSF profiles in the absence of any CTE loss, while green lines indicate schematic CTI-induced PSF profiles, showing the effect of CTI-induced photometric loss and centroid shifts ΔY .

During the readout process the charge is trapped and released on different time scales. The trapping of charge during the readout causes errors in the measurement of the object flux and its position. The release of deferred charges causes a faint tail to appear on each object, thus obscuring the real position and flux of the object and increasing the noise in the image. The effect of errors in the measurements of the object flux and positions due to the CTE loss (in the dominant parallel direction) in the two WFC3 UVIS chips is schematically illustrated in Figure 2. The black profile is the Point Spread Function (PSF) from a source not impacted by CTE degradation. The green profile is the CTI-impacted PSF where the peak intensity is decreased and the centroid is shifted by a certain amount (ΔY) in the direction away from the readout amplifier (ABCD). As a result in UVIS1, the centroid is shifted downwards away from the amplifiers A & B and peak intensity is more decreased far away from the amplifiers. It is opposite for UVIS2, where the readout amplifiers C & D are at the bottom: the centroid is shifted upwards away from amplifiers and the peak intensity is more decreased far away from the amplifiers.

3.2. Aperture Photometry

The first step in the analysis of the CTE is to measure the flux and position of each star in each chip and in each exposure. Because the PSF of WFC3 /UVIS is under-sampled and similarly to ACS/WFC, varies across the CCD chip, the PSF may suffer from systematic errors, which in turn affect the flux and positional measurement of a star, depending on its location on the chip. The IRAF/DAOPHOT/PHOT task, which includes a 2-D Gaussian fit to the PSF centroid and simultaneous aperture photometry, was used to obtain the flux, X and Y positions of stars on each of the UVIS CCD chips in all 36 images (12 images \times 3 epochs). Aperture photometry was performed with the range of radii between 1 and 10 UVIS pixels and a sky annulus with inner radius of 10 pixels and width of 5 UVIS pixels.

A 2-D Gaussian fit to the X and Y positions as a function of instrumental magnitude shows a good formal measuring accuracy even for the under-sampled UVIS PSF. As seen in Figure 3, the distribution of the formal X & Y errors versus instrumental magnitudes show not only well measured stars but also the cloud of spurious detections such as cosmic rays and hot pixels. The points above the astrometric errors trend ($\sigma_{XY} \gtrsim 0.05$ for $-5.0 \lesssim \text{mag} \lesssim 0$) are cosmic rays, while the points above the astrometric trend ($\sigma_{XY} \gtrsim 0.2$ for $-2.0 \lesssim \text{mag} \lesssim 2.0$) are hot pixels.

In order to avoid spurious detections, the X & Y positions of the stars from short exposures have to be matched with the same stars from long exposures. To do so, the measured positions from the WFC3/UVIS flat-fielded (`*flt.fits`) images were corrected for geometric distortion by applying the WFC3/UVIS geometric distortion coefficients from Kozhurina-Platais *et al.* (2009) and then the X, Y positions of stars in the short exposure were matched to stars in the long exposure taken in the same pointing using the tolerance

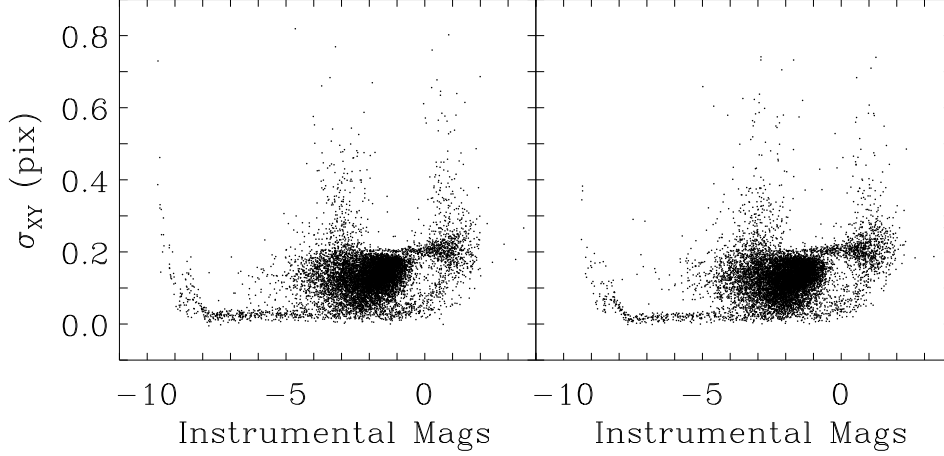


Fig. 3.— Centering errors of X & Y positions as a function of instrumental magnitude for stars in F606W images of NGC6791 in UVIS2 (left panel) and UVIS1 (right panel). The points above the astrometric error trend ($\sigma_{XY} \gtrsim 0.05$ for $-5.0 \lesssim \text{mag} \lesssim 0$) are likely to be cosmic rays. The stars brighter than about -8 instrumental magnitude are saturated. The positional errors (σ_{XY}) are calculated as $\sqrt{\sigma_X^2 + \sigma_Y^2}$.

of 0.2 pixels. If the tolerance is too large, the cosmic rays and hot pixels will be included in the CTE analysis.

Figure 4 shows the color - magnitude diagram (CMD) of NGC6791 derived with aperture photometry from single observations through the F606W and F502N filters with long exposures (360 sec and 460 sec respectively). The left panel of Figure 4 shows the CMD for all measured stars, matched with tolerance of $\lesssim 1.0$ pixels. The extremely blue population, with color in the range of $-5.0 \lesssim B-V \lesssim -2.0$ and magnitude $V \lesssim 23$ are hot pixels matched between the F606W and F502N images, and the population with the color in the range of $-0.5 \lesssim B-V \lesssim 2.5$ is the main sequence (MS) of NGC6791 with the MS turn-off at $V=17.5$ magnitudes. The right panel of Figure 4, presents the stars measured in the F606W and F502N images matched with a tolerance of 0.2 pixels, and does not show any indication of contamination by cosmic rays and/or hot pixels. Thus, the tolerance of 0.2 pixels is small enough to avoid spurious detections such as cosmic rays and hot pixels, and yet large enough to allow a robust measurement of the CTI-induced centroid shifts. The color-magnitude diagram of NGC6791 (Figure 4, the right panel), shows a narrow MS with several faint stars from the background and has a wide magnitude range, ~ 5.5 magnitudes below the main sequence turn-off, and 2.5 magnitudes range in color. The wide magnitude range and $\lesssim 1000$ stars per UVIS image are sufficient for the analysis of the CTI-induced losses.

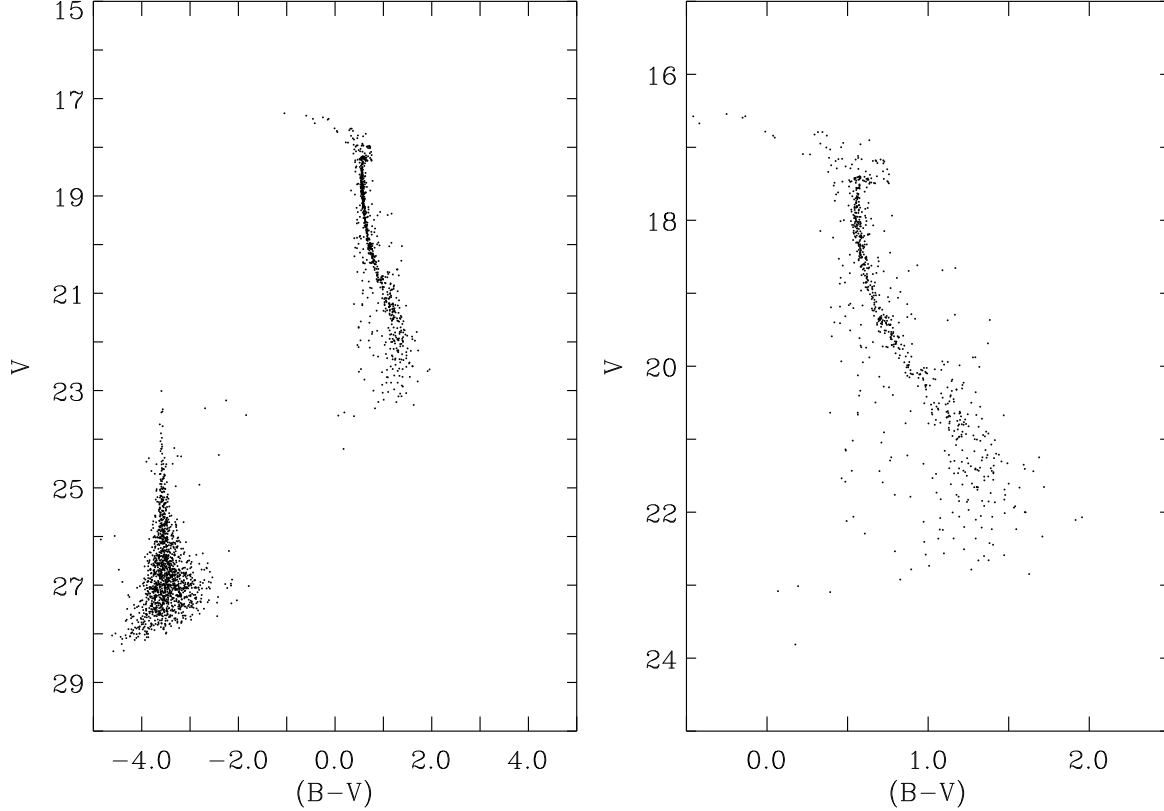


Fig. 4.— Color Magnitude Diagram of open cluster NGC6791 in Vega System. Left panel shows all measured objects in long exposures taken through F502N and F606W filters. Right panel shows only stars matched with the tolerance of ~ 0.2 pixels. The main sequence of NGC6791 has a wide range in magnitudes (~ 6) and reaches down to 23th magnitude.

4. CTE Effects in WFC3/UVIS Flat-Fielded Images

4.1. Photometric Flux Loss in F606W

In order to properly identify and quantify the CTI-induced flux loss, we compared aperture photometry results derived from 3-pixels radii aperture from flat-fielded images taken with short and long exposures. We define the instrumental magnitude as $-2.5 \times \log_{10}(\frac{FLUX}{EXPTIME})$, where $FLUX$ is the signal from the star (in e^-) as given by the aperture photometry formalism, and $EXPTIME$ is the exposure time in seconds.

The “residual magnitude” is defined as:

$$\Delta \text{Mag} \equiv \text{Mag}_{\text{long}} - \text{Mag}_{\text{short}} \quad (1)$$

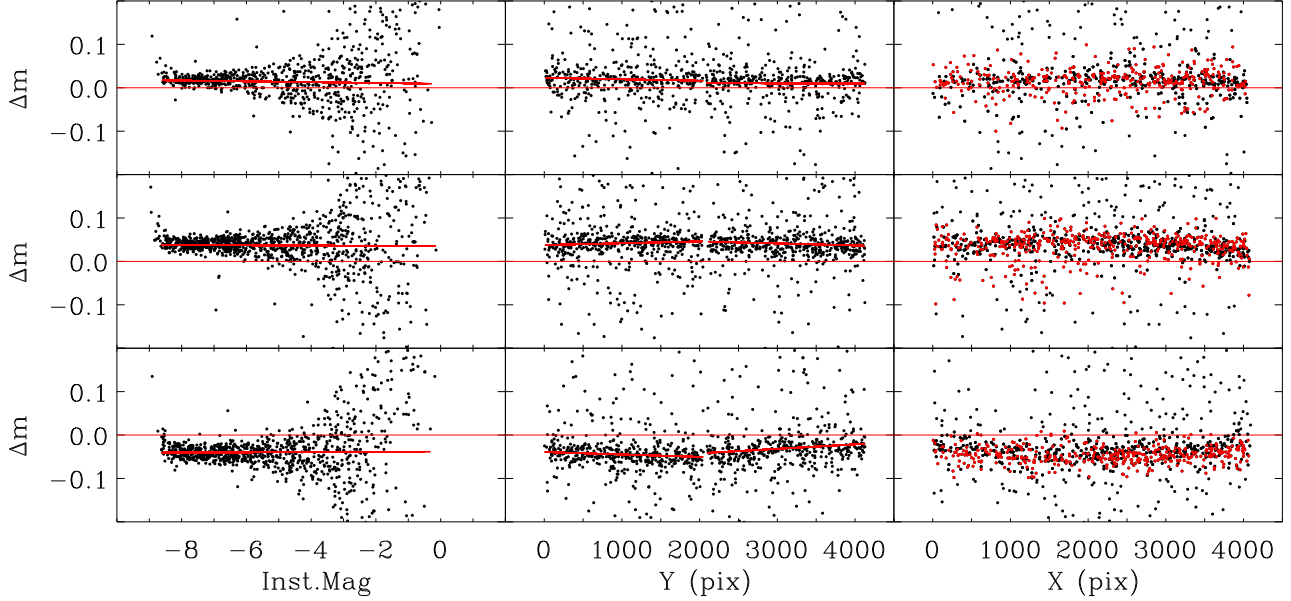


Fig. 5.— Difference between instrumental magnitudes derived from short and long exposures of NGC6791 as function of instrumental magnitude (from the long exposure), ΔMag as function of Y and X position (from left to right respectively) for filters F606W, taken in October 2009. From top to bottom, the residuals of magnitude from images with postarc $81''\!:\!6''$, $0\!:\!81''$ and $0\!:\!0$ respectively. The over-plotted solid red line is the linear fit representing the trend in magnitude residuals as function of instrumental magnitude (the first columns on the left). The second columns, the over-plotted solid red line is the linear fit representing the trend in magnitude residuals as function of Y positions for UVIS2 and UVI1. The third columns, ΔMag as function of X , show the stars from UVIS1 as red dots and black are stars from UVIS2.

For each pair of short-long F606W exposures from all CAL-11924 observations, we plot ΔMag as function of instrumental magnitude from the long exposures, and ΔMag as function of X and Y positions (see Figures 5 through 7). As can be seen in Figure 5, there are an offsets in ΔMag as function of instrumental magnitude from long exposures, as well as X and Y position. The offsets in ΔMag change from one pointing to another over one HST orbit and is constant for all stars from bright to faint. According to Riess & Mack (2004) and Goudfrooij *et al.* (2006), ΔMag is known to be more negative with

decreasing source signal as expected for CTE-induced photometric losses. However, for the WFC3/UVIS observations from September 2009, March 2010 and September 2010, ΔMag is mostly constant for all stars from bright to faint, as can be seen in Figure 5, 7 and 8. It is important to notice here, that only in one set of data, observations from September 2010, ΔMag as function of Y positions (Figure 7, the bottom panel in the middle) shows some evidence for photometric losses in the Y direction. The solid red line in the bottom middle panel of Fig. 7 shows that the trend of ΔMag versus Y position has different slopes for the different UVIS CCD chips (UVIS1 versus UVIS2), resembling a “V” shape (see Kozhurina-Platais *et al.* 2007). These differences are due to the fact (see Figure 2) that the readout amplifiers for the UVIS chips are located at row 1 (for the UVIS2 chip) and row 4096 (for the UVIS1 chip), i.e., the readout directions for the two chips are opposite to each other.

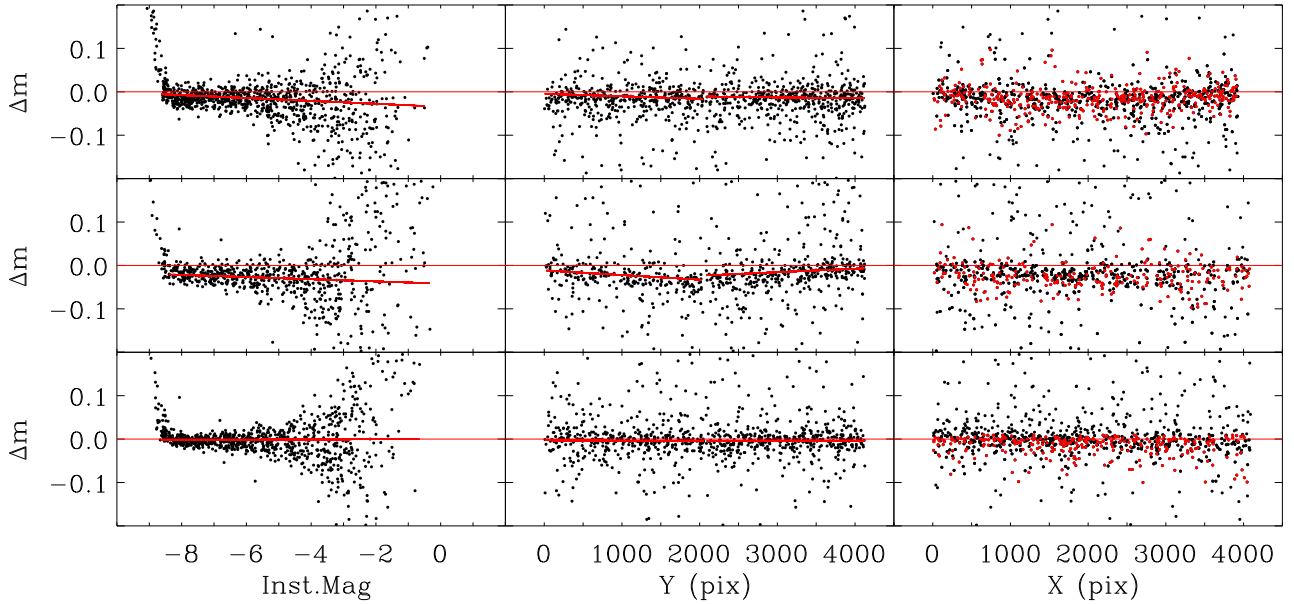


Fig. 6.— The same as Figure 5 only for observations taken in March 2010.

Thus, the detailed examination of the magnitude residuals between short and long exposures over one year of CTE external observations, has shown the value of ΔMag (see Figure 5, 6, 7) is changing from one pointing to another during one HST orbit when using aperture radius of 3 pixels. It is important to notice here, that during one HST orbit there is evidence of CTE for one pointing and there is no evidence for CTE in another. Does ΔMag correlate with the background levels, and/or with the time and date the observations were taken? To answer these questions, the information of the sky background level, ΔMag and the time and date of observations, are provided in the Table 2 for each of the F606W

images from CAL-11924 calibration program.

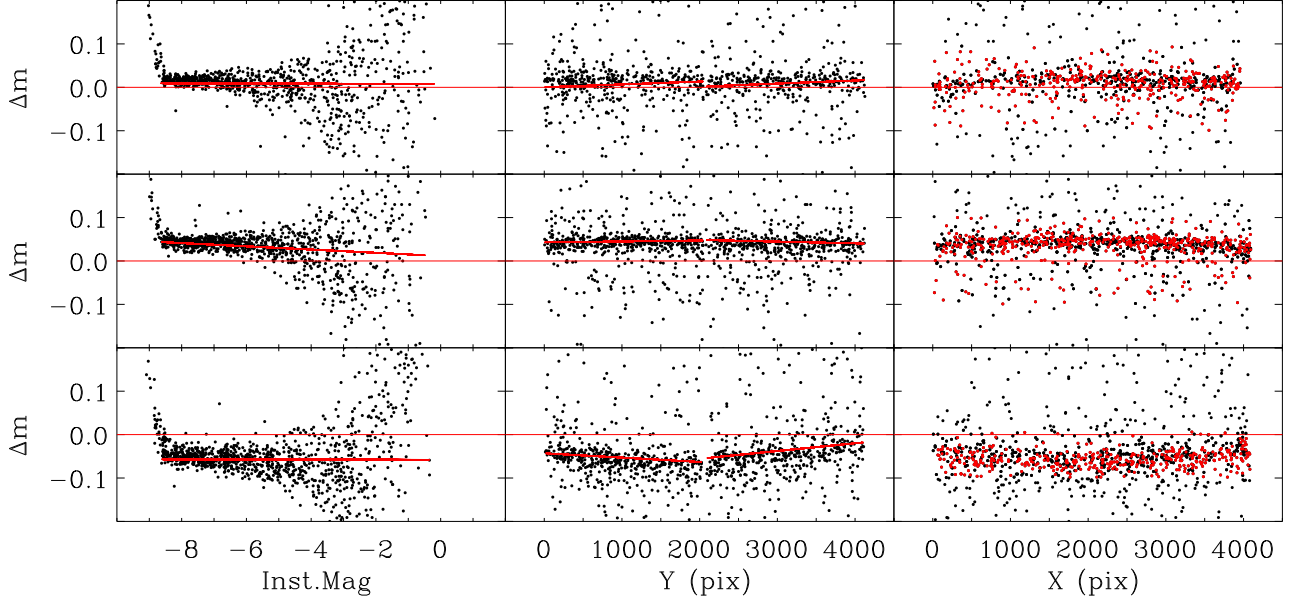


Fig. 7.— The same as Figure 5 only for observations taken in September 2010.

Table 2: Average sky background, the time and date of F606W observations.

Image pairs	Exp. Time (sec)	Sky value (e^-)	Δ Mag	Time (hh:mm:ss)	Date (yy:mm:dd)
ibc601h0q–ibc601h5q	30–360	1.1–16.8	0.016	04:57:48–06:15:39	2009:10:02
ibc601gzq–ibc601h3q	30–360	1.1–30.6	0.037	04:55:06–06:07:31	2009:10:02
ibc601gxq–ibc601h2q	30–360	1.5–13.9	-0.036	04:41:14–05:11:38	2009:10:02
ibc602v4q–ibc602v9q	30–360	1.3–17.2	-0.014	19:37:25–20:07:25	2010:03:25
ibc602v3q–ibc602v7q	30–360	1.3–14.6	-0.025	19:34:43–19:59:23	2010:03:25
ibc602v1q–ibc602v6q	30–360	3.8–14.6	-0.003	18:51:24–19:51:15	2010:03:25
ibc603zpq–ibc603zuq	30–360	1.2–18.1	0.002	08:15:03–09:32:54	2010:09:02
ibc603zoq–ibc603zsqu	30–360	1.2–33.4	0.035	08:12:21–09:24:46	2010:09:02
ibc603zmq–ibc603zrq	30–360	1.7–13.8	-0.056	07:58:29–08:28:53	2010:09:02

From Table 2, one can see that there is no evidence of a correlation between Δ Mag and the sky background level, time or date of the observations were taken. A possible cause for a systematic photometric offset could be changes in the PSF due to focus variations (“orbital breathing”) as a result of changes in the thermal environment of HST over

the orbit. The analysis presented in this report is based on a differential comparison of photometry between short/long exposure pairs, and any significant focus difference between the two images of a given pair could systematically affect the results, particularly for small apertures. To determine whether this may be the case here, an average focus was computed for each image based upon a breathing model (data from C.Cox 2010). The magnitude residuals were plotted as function of the difference in focus between the short and long exposures. As can be seen in Figure 8, image pairs that show higher residual magnitude offsets were found also to show a generally higher difference in focus setting (difference $\lesssim -2$ or $\gtrsim +3$).

Thus, the global offsets in photometry between long–short exposures as a function of instrumental magnitude, X and Y are likely due to thermal effects over the course of the HST orbit.

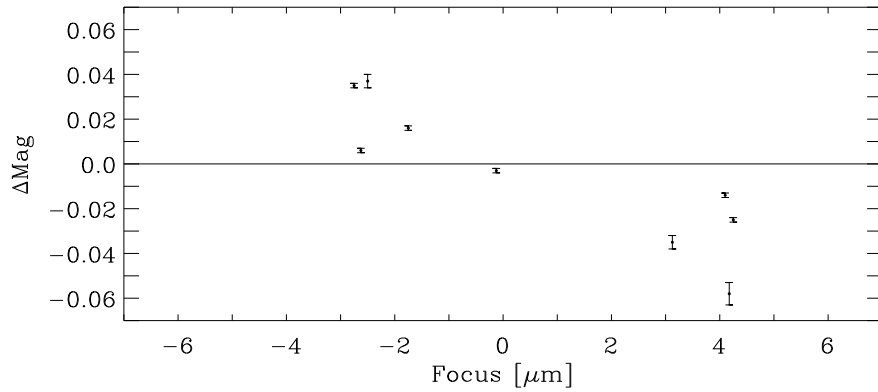


Fig. 8.— Residual magnitude offset ΔMag as a function of the WFC3/UVIS focus difference between the short and long exposure of each image pair. The WFC3/UVIS focus in microns.

Thus, to improve the accuracy of the total flux measurement one must measure stars using a sufficiently large aperture so that the fraction of light missed by guiding errors, focus change or CTE induced losses, will be included in the given aperture radius. As described in Sec.3.2, aperture photometry was performed with serial consecutive radii of 1, 2, 3, 4, 5, 6, 7, 8, 9, 10 UVIS pixels and a sky annulus with radius of 10 and width of 5 pixels. Figure 9 shows the radial profile of well-measured stars in one NGC6791 image taken through the F606W filter, where the consecutive aperture radii and sky annulus are over-plotted. As can be seen in Figure 9, a radius of 5 UVIS pixels contains most of the total flux of the star and the star profile disappears into the sky background.

According to Stetson (1987), the definition of the best aperture radius is:

$$R_{\text{aperture}} = 2.0 \times FWHM + 1.0 \quad (2)$$

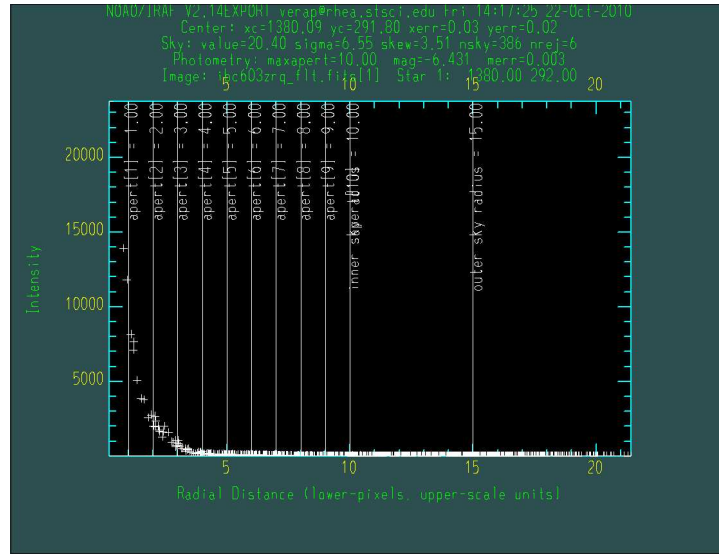


Fig. 9.— Radial profile of well-measured stars in one NGC6791 image taken through the F606W filter: the consecutive aperture radii and location of sky annulus are over-plotted.

The FWHM of the WFC3/UVIS PSF is, on average, ~ 2 pixels and thus, according to Equation 2, an optimal aperture for the UVIS would be ~ 5 pixels. Also, as shown in the curve-of-growth in Figure 10, the magnitude difference between successive apertures as a function of aperture radius asymptotically approaches a maximum at radius of 5 pixels and begins to diverge thereafter.

Figure 11 shows, from left to right, ΔMag as a function of 1) instrumental magnitude, 2) Y position, and 3) X position as measured with a 5pixels radius aperture on September 2010 observations. Compared to the photometry with radius of 3 pixels shown in Figure 7, the photometric results are much improved. The average scatter between short–long exposures is now about half of what it was. In addition, there are no longer any systematic magnitude-independent offsets in the three sets of data and there is no evidence CTE loss

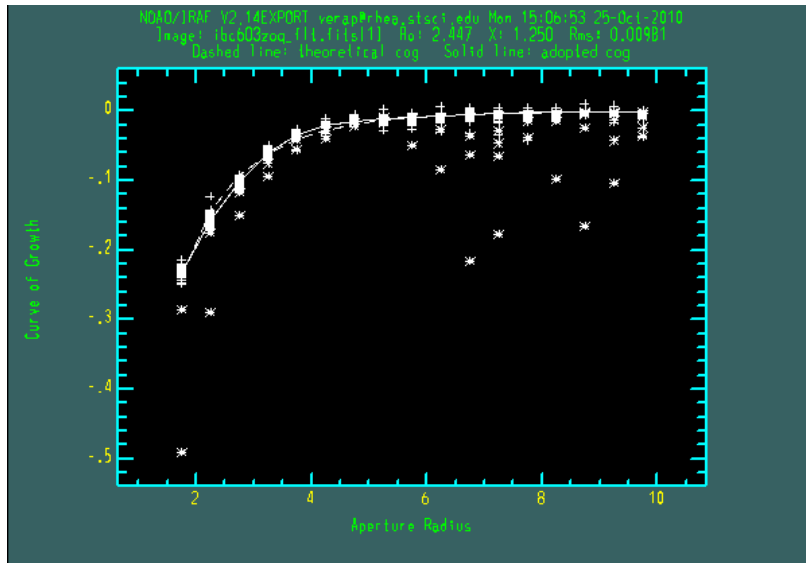


Fig. 10.— Curve-of-growth for the WFC3/UVIS.

in the plots of ΔMag as function of instrumental magnitude and X and Y position. These results show that the large offset from +3% to -5% in the photometry in Figure 7 is mostly due to the PSF change during one HST orbit. While aperture photometry is one of the simplest ways to measure fluxes, it does not take into account any changes to the PSF, either temporal (during the HST orbit) or spatial (across the chips). An alternative method would be to use an *effective* PSF fitting technique similar to WFPC2 (Anderson & King, 2000) and ACS/WFC (Anderson & King 2006). In this method, variations of the PSF across the UVIS chips are represented by a 7×8 array of fiducial PSFs, with interpolation for intermediate positions. According to Anderson (2010), in general the WFC3 PSF varies more slowly with position (typically 5-10%) than it does in ACS data (typically 15% or worse, primarily due to charge diffusion). The variation of the PSF with time due to (e.g.) telescope breathing is represented within the ePSF as a spatially-constant perturbation to the PSF and usually introduces a $\pm 15\%$ variation. The ePSF method fits the innermost 5×5 pixels of the target stars; the default output magnitudes are normalized to a radius of 10 UVIS pixels, the aperture used for UVIS flux calibration (e.g., Kalirai et al. 2010).

The ePSF method was used on the three sets of WFC3/UVIS data and compared the results with those obtained from aperture photometry. As seen in Figure 12, the photometry obtained with ePSF fitting and perturbation to the PSF shows that systematic large Δ Mag offsets due to breathing-induced PSF changes have been reduced, but the photometric scatter is larger compared to photometry derived from 5 pixels radius aperture. The large scatter in the photometric residuals is persistent across the entire range of magnitudes. Thus, for the CTE analysis, aperture photometry with a radius of 5 pixels is preferred.

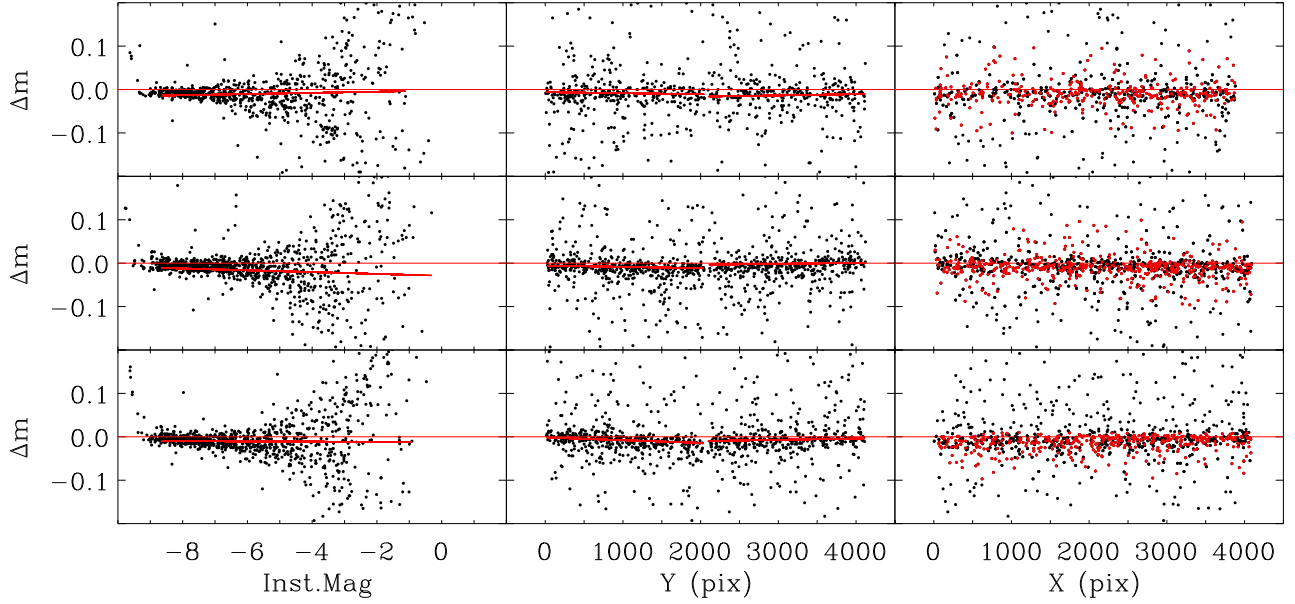


Fig. 11.— The same as Figure 7 for F606W observations taken in September 2010. Photometry derived with aperture radius of 5 UVIS pixels and to be compared with aperture photometry of 3 UVIS pixels.

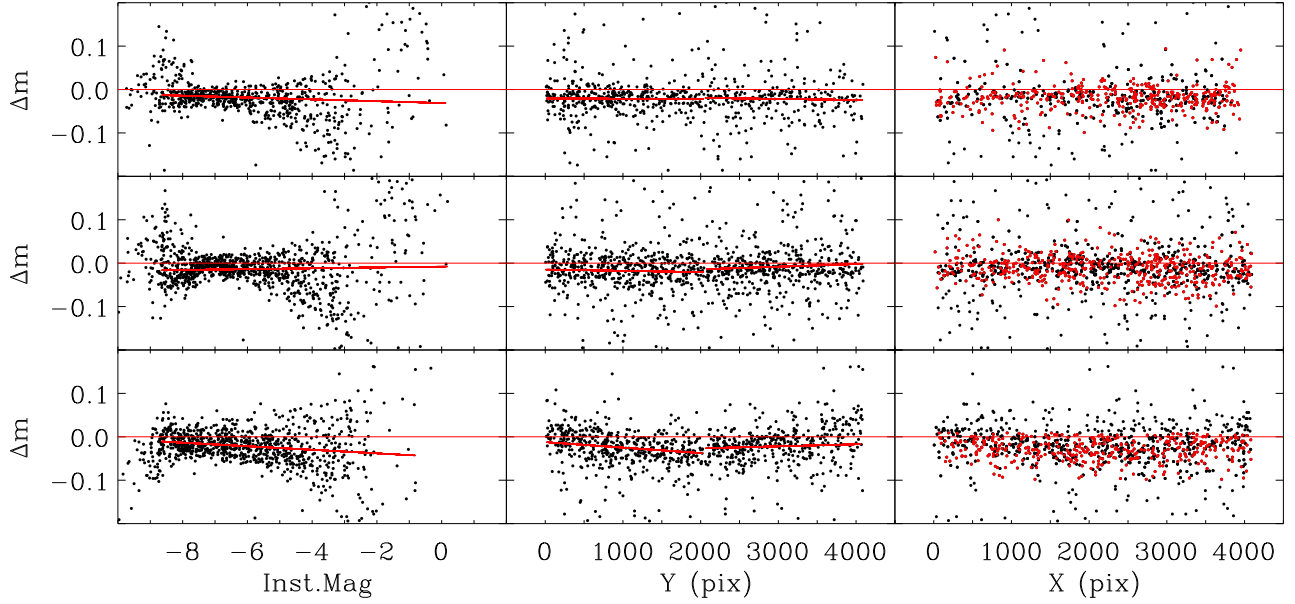


Fig. 12.— The same as Figure 7 for F606W observations taken in September 2010. Photometry derived with ePSF fitting technique and to be compared with aperture photometry of 3 and 5 UVIS pixels.

4.2. Photometric Flux Loss in F502N

Aperture photometry with a radius of 5 pixels was performed on images taken through the F502N filter. The throughput at F502N is only 2.2% of the F606W filter, because of that the low sky background and stellar flux in F502N will be more sensitive to CTE losses. The photometric results for data taken in September 2010 are shown in Figure 13, which indicate the magnitude residuals between short and long exposures at about -0.04 magnitude. Furthermore, ΔMag *vs.* versus instrumental magnitude is not constant. It becomes more negative with decreasing source signal, as might be expected for CTI-induced flux losses. The evidence for CTI-induced photometric losses is more pronounced in the ΔMag versus Y positions, resembling of a “V” shape, due to the opposite readout directions.

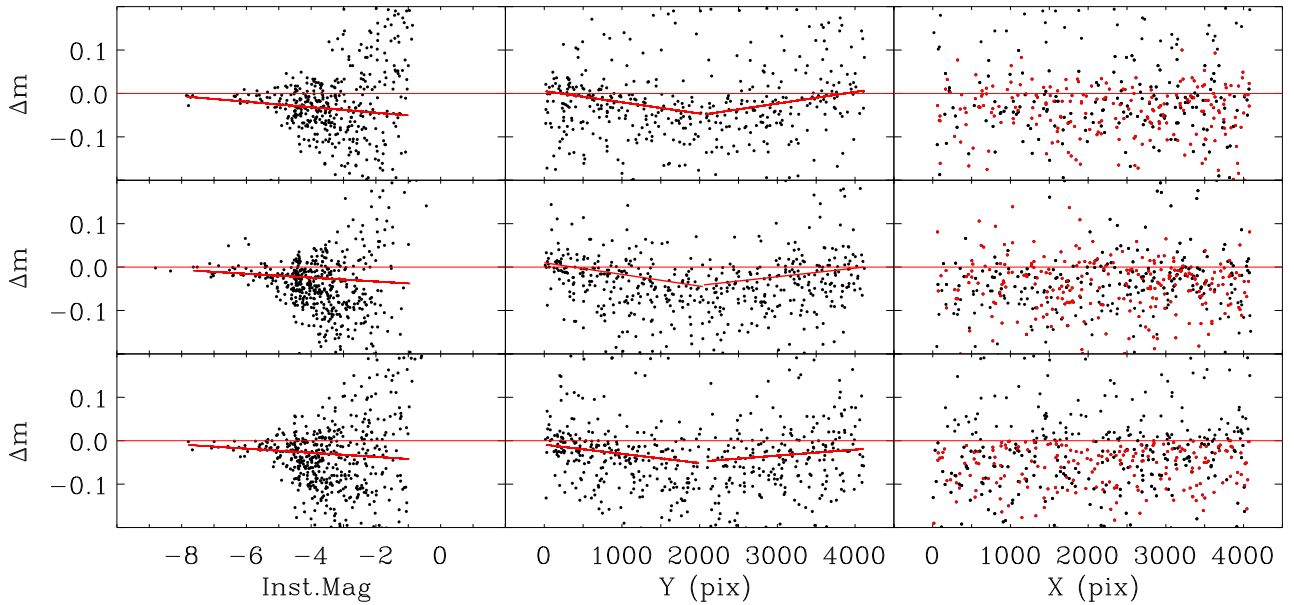


Fig. 13.— Difference between instrumental magnitudes derived from short and long exposures of NGC6791 as function of instrumental magnitude (from the long exposure), ΔMag as function of Y and X position (from left to right respectively) for filter F502N, taken in September 2010. From top to bottom, the residuals of magnitude from images with postarc 81'' : 6'', 0 : 81'' and 0 : 0 respectively. The over-plotted solid red line is the linear fit representing the trend in magnitude residuals as function of instrumental magnitude (the first columns on the left). The second columns, the over-plotted solid red line is the linear fit representing the trend in magnitude residuals as function of Y positions for UVIS2 and UVI1. The third columns, ΔMag as function of X , show the stars from UVIS1 as red dots and black are stars from UVIS2.

The average sky background, Δ Mag offset, time and date of the observations taken through the F502N filter are provided in Table 3.

Table 3: Average sky background, the mean of Δ Mag, Time & Date of F502N observations.

Image pairs	Exp. Time (sec)	Sky value (e^-)	Δ Mag	Time (hh:mm:ss)	Date (yy:mm:dd)
ibc601gqq–ibc601gvq	60–420	0.01–1.08	-0.001	04:57:48–06:15:39	2009:10:02
ibc601goq–ibc601gtq	60–420	0.07–0.93	-0.015	04:55:06–06:07:31	2009:10:02
ibc601gmq–ibc601grq	60–420	0.03–0.64	-0.017	04:41:14–05:11:38	2009:10:02
ibc602uuq–ibc602uzq	60–420	0.01–0.67	-0.028	19:37:25–20:07:25	2010:03:25
ibc602usq–ibc602uxq	60–420	0.01–0.97	-0.027	19:34:43–19:59:23	2010:03:25
ibc602urq–ibc602uvq	60–420	0.03–1.19	-0.021	18:51:24–19:51:15	2010:03:25
ibc603zfz–ibc603zfq	60–420	0.10–1.28	-0.036	08:15:03–09:32:54	2010:09:02
ibc603zdz–ibc603ziz	60–420	0.11–0.58	-0.031	08:12:21–09:24:46	2010:09:02
ibc603zdz–ibc603ziz	60–420	0.11–0.58	-0.037	07:58:29–08:28:53	2010:09:02

As seen in Table 3, the sky background for the F502N images is quite low, in the $0.1\text{--}1\ e^-$ range, compared to the F606W images (Table 2) which have sky backgrounds in the $1\text{--}30\ e^-$ range. Background plays a significant role in CTI: a higher background fills traps, thereby reducing the amount of flux that will be lost during the readout. In fact, to take advantage of this effect, some instruments (ACS/WFC for example) are designed with preflash, postflash, and or charge injection capability in order to mitigate CTI effects. The WFC3/UVIS camera has the latter capability, expected to be made available as an option for observers in Cycle 19.

Thus, to assess the state of the WFC3/UVIS CTI-induced losses during the first year on-orbit, we focus on images with low background level, taken through the F502N filter, and use the radius of 5 pixels aperture photometry results. The CTI-induced photometric losses generally are characterized by the flux (in e^-) because of that instead of magnitude residuals between long and short exposures, the ratio of flux between long and short is used presented as follows:

$$\delta(Flux) = \frac{FLUX_{long}}{FLUX_{short}} \bigg/ \frac{EXPTIME_{long}}{EXPTIME_{short}} \quad (3)$$

where $FLUX_{long}$, $FLUX_{short}$ are measured fluxes from the long and short exposures (in e^-) and $EXPTIME_{long}$, $EXPTIME_{short}$ are the long and short exposure time in seconds.

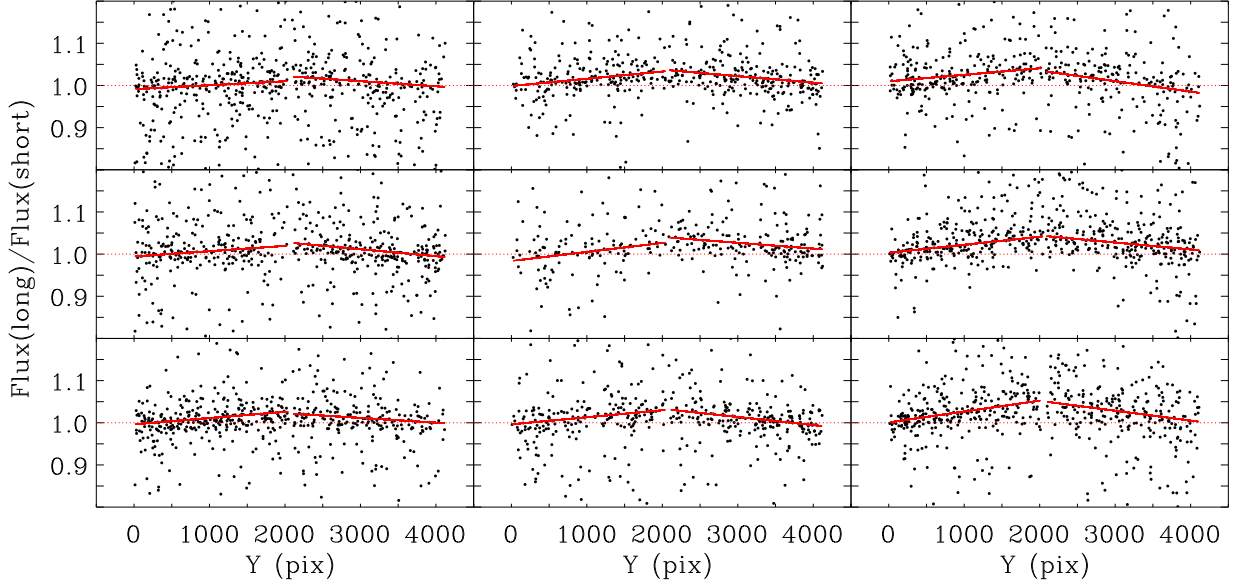


Fig. 14.— Flux ratio *vs.* Y positions for all observations through the F502N filters. From left to right are the plots for October 2009, March 2010, September 2010 observations. From top to bottom the flux ratio from three different postarg - $81'' : 6''$, $0 : 81''$ and $0 : 0$ respectively. The over-plotted solid red lines are the linear fits of flux ratio as function of Y positions for UVIS2 chip ($Y \lesssim 2051$) and for UVIS1 chip ($Y \gtrsim 2051$). The Y positions are given in WFC3/UVIS pixels.

Figure 14 shows the flux ratio $\delta(Flux)$ calculated from Eq.(3) as function of Y position for all observations from October 2009, March 2010 and September 2010. The flux ratio shows strong evidence of photometric losses in Y direction and a different CTI slope, for each of the two CCD chips, resulting in the previously described “V” shape due to the opposite readout directions for UVIS1 and UVIS2 CCD chips.

In order to properly identify and quantify the WFC3/UVIS CTE-induced loss, we select the appropriate stars by following three criteria:

- within the magnitude range from short exposures $-3.85 \lesssim \text{Ins.Mag}_{F502N} \lesssim -2.35$ which corresponds to the flux range $552.6 \lesssim \text{Flux}_{short} \lesssim 2081.4$ (in e^-), i.e. the stars with low signal;
- in the range of Y positions for UVIS2: within the Y range of $0 \lesssim Y \lesssim 500$ and $1551 \lesssim Y \lesssim 2051$ (close and far, respectively, from the C & D amplifiers);
- in the range of Y positions for UVIS1: within the Y range of $2051 \lesssim Y \lesssim 2551$ and $3500 \lesssim Y \lesssim 4096$ (close and far, respectively, from the A & B amplifiers).

The CTE loss for each UVUS chip is calculated as the mean of the $\delta(flux)$ (Eq.3) for stars farthest from the amplifier minus the mean of the $\delta(flux)$ for stars nearest the readout amps. The CTE losses in the WFC3 CCDs from each image pair in the three epochs are presented in Table 4. The number of stars for each Y range used for calculation of the CTE losses are reported in Table 4. Though some scatter within each epoch is presented, as expected these low-sky background data exhibit a clear trend for increasing CTI over time, from 2.5% in the fall of 2009 to 7% in the fall of 2010.

Table 4: The WFC3/UVIS CTE loss measured in the F502N observations.

Image pairs	UVIS2 (%)	Number Stars	UVIS1 (%)	Stars Number	Date (yy:mm:dd)
ibc601gqq–ibc601gvq	2.1±0.7	19/15	2.4±0.9	14/18	2009:10:02
ibc601goq–ibc601gtq	2.4±0.5	11/17	1.7±0.4	9/16	2009:10:02
ibc601gmq–ibc601grq	2.9±0.5	20/23	3.1±0.5	14/11	2009:10:02
ibc602uuq–ibc602uzq	4.1±0.5	11/10	4.7±0.3	13/12	2010:03:25
ibc602usq–ibc602uxq	4.9±0.4	7/7	5.1±0.6	10/10	2010:03:25
ibc602urq–ibc602uvq	4.6±0.5	14/10	3.8±0.7	7/20	2010:03:25
ibc603zfq–ibc603zkq	7.7±0.7	14/21	5.7±0.3	10/8	2010:09:02
ibc603zdq–ibc603ziq	4.8±0.3	10/21	4.6±0.5	11/14	2010:09:02
ibc603zcq–ibc603zgq	9.9±0.5	18/24	7.8±0.5	18/24	2010:09:02

Similar to CTI-induced losses calculated from the observations through the F502N filter with low background, we also assess the state of CTI-induced losses from images with high background ($1\text{--}30e^-$), taken through F606W. The calculation of CTI in F606W images is similar to those described for F502N images. Table 5, listed the CTI-induced losses in the F606W filter from each image pair in three epochs.

Table 5: The WFC3/UVIS CTE loss measured in the F606W observations.

Image pairs	UVIS2 (%)	Number Stars	UVIS1 (%)	Stars Number	Date (yy:mm:dd)
ibc601h0q–ibc601h5q	1.4±0.9	18/12	1.6±0.4	11/18	2009:10:02
ibc601gzq–ibc601h3q	0.8±0.5	20/13	0.3±0.8	15/12	2009:10:02
ibc601gxq–ibc601h2q	1.6±0.4	11/11	1.2±0.6	15/15	2009:10:02
ibc602v4q–ibc602v9q	1.1±0.5	16/16	1.1±0.6	17/10	2010:03:25
ibc602v3q–ibc602v7q	1.2±0.6	16/10	0.8±0.6	19/14	2010:03:25
ibc602v1q–ibc602v6q	0.6±0.4	12/11	2.6±0.7	10/11	2010:03:25
ibc603zpq–ibc603zuq	6.3±0.4	16/18	3.2±0.7	13/14	2010:09:02
ibc603zoq–ibc603zsq	0.5±0.5	15/10	1.4±0.8	14/10	2010:09:02
ibc603zmq–ibc603zrq	1.4±0.3	15/17	2.6±0.7	11/14	2010:09:02

The F606W images, with high background ($1\text{--}30e^-$), show large scatter in the calculated CTE loss within each epoch and from epoch to epoch. The average of three pairs of images in each epoch shows that CTE loss is ranged from 1% in October 2009 to 2% in the fall 2010. The large scatter in the WFC3/UVIS CTE loss in both cases could be explained by large uncertainties in the flux measurements for faint stars and by low numbers of faint stars, which lead to large uncertainties in the calculation of CTI loss.

5. Conclusion

In this paper we report the first CTE evaluation based on external calibration observations from the new instrument *Wide Field Camera 3* (WFC3). The observations of the rich open cluster NGC6791 were started soon after the servicing mission and continued through the first year of WFC3. These early observations (CAL-11924, PI Kozhurina-Platais) have been used to provide a preliminary assessment of the WFC3/UVIS CTE and its time dependence. Imperfect Charge Transfer Efficiency is likely the most important instrument issue affecting photometry with the WFC3/UVIS. As discussed in Sec.4.2 the low-sky background observations exhibit a clear trend for increasing WFC3/UVIS CTI over time. From October 2009, to the fall of 2010, the WFC3/UVIS CTE decreased from 2% to 7% for sources in the flux range in $500e^-$ – $2000e^-$. This is a relatively large and unexpected CTE loss, a factor of 2–3 greater than expected from ACS/WFC in its first years on orbit in 2002-2003 (Chiaberge *et al.* 2009)

The WFC3/UVIS CTE degradation will continue to be monitored with both internal and external observations. Additional observations of NGC6791 and 47Tuc (CAL-12379, PI K. Noeske) planned for the fall of 2010 and spring of 2011, will be used to develop formal photometric and astrometric corrections for WFC3 science data.

One option for mitigation of CTI can be achieved by invoking the WFC3 charge injection capability (CAL-12348, PI S. Baggett). Analogous to a pre-flash mode, the charge is injected before the science observation, albeit electronically rather than optically, in order to temporarily fill the traps causing the CTI. There will be a noise penalty, although it is expected to be significantly lower ($\sim 15e^-$ for 17,000 e^- injection in the CI rows) than photon shot noise (Giavalisco 2003, Bushouse *et al.* 2011). The charge injection capability is expected to be made available as an observing option in Cycle 19.

Acknowledgments

We thank Colin Cox for providing the focus information for these observations, Thomas Wheeler for SAA passage information, and Peter McCullough, Larry Petro, and Adam Riess for helpful discussions during the development of the APT Phase II of the proposal. V.K.-P. is grateful to Jay Anderson for sharing his eSPF fitting code. V.K.-P. is also

thankful to Bryan Hilbert for reading the first draft of this paper.

References

- Anderson, J., King, I., 2000, PASP, 112, 1360
- Anderson, J., King, I., 2006, ACS Instrument Science Report 2006-01 (Baltimore: STScI)
- Anderson, J., Bedin, L., 2010, PASP
- Anderson, J., 2010 (in private communication)
- Bushouse, H., *et al.* 2011, WFC3 Instrument Science Report 2011-02 (Baltimore:STScI) (in print)
- Dressel, L., *et al.* 2010, "Wide Field Camera 3 Instrument Handbook, Version 2.0" (Baltimore: STScI)
- Chiaberge, M., Riess, A., Mutchler, M., Sirianni, M., & Mack, J., 2006, in "2006 HST Calibration Workshop", eds. A. Koekemoer, P. Goudfrooij, & L. Dressel,(Baltimore:STScI)
- Chiaberge, M., Lim, P.M., Kozhurina-Platais, V., Sirianni, M., Mack, J., 2009, ACS Science Instrument Report 2009-01, (Baltimore: STScI)
- Dolphin, A. E., 2000, PASP, 112, 1397
- Giavlisco, M., 2003, WFC3 Science Instrument Report 2003-01, (Baltimore: STScI)
- Gilliland, R., Goudfrooij, P., Kimble, R., 1999, PASP, 111, 1009
- Goudfrooij, P., & Kimble, R. A., 2003, in "2002 HST Calibration Workshop", eds. A. Arribas, A. Koekemoer, & B. C. Whitmore (Baltimore: STScI), p.105
- Goudfrooij, P., Bohlin, R. C., & Maíz Apellániz, J., 2006, PASP, 118, 1455
- Kalirai, J., Bagget, S., Borders, T., Rajan, A., 2010, WFC3 Science Instrument Report, 2010-14, (Baltimore:STScI)
- Koekemoer, A.,M., Fruchter, A., Hook, R. N., & Hack, W., 2002, in "2002 HST Calibration Workshop", eds. A. Arribas, A. Koekemoer, & B. C. Whitmore (Baltimore: STScI), p.337
- Kozhurina-Platais, V., Goudfroij P., Puzia, T., 2007, ACS Science Instrument Report 2007-04, (Baltimore: STScI)
- Kozhurina-Platais, V., Sirianni, M., Chiaberge, M., 2008, in "Proceedings of IAU Symposium", Vol. 248, p.272-273
- Kozhurina-Platais, V., *et al.*, 2009, WFC3 Science Instrument Report 2009-34, (Baltimore: STScI)
- Mutchler, M., & Sirianni, M., 2005, ACS Science Instrument Report 2005-17 (Baltimore: STScI)
- Riess, A., 2003, ACS Science Instrument Report 2003-09 (Baltimore: STScI)
- Riess, A., & Mack, J., 2004, ACS Science Instrument Report 2004-06 (Baltimore: STScI)
- Stetson, P., 1987, PASP, 99, 191
- Whitmore, B. C., Heyer, I., & Casertano, S., 1999, PASP, 111, 1539

Appendix A

Table 1: The list of NGC6791 observations taken with the WFC3 UVIS channel.

Image ID	POSTARG1 (")	POSTARG2 (")	Filter	Exp.time (sec)	Time of Obs (hh:mm:ss)	Date (yy-mm-dd)
ibc601gmq	0.00	0.00	F502N	60.0	03:00:51	2009-10-02
ibc601goq	0.00	81.59	F502N	60.0	03:04:03	2009-10-02
ibc601gqq	81.00	6.10	F502N	60.0	03:18:25	2009-10-02
ibc601grq	0.00	0.00	F502N	420.0	03:21:35	2009-10-02
ibc601gtq	0.00	81.59	F502N	420.0	03:30:43	2009-10-02
ibc601gvq	81.00	6.10	F502N	420.0	04:31:41	2009-10-02
ibc601gxq	0.00	0.00	F606W	30.0	04:41:14	2009-10-02
ibc601gzq	0.00	81.59	F606W	30.0	04:55:06	2009-10-02
ibc601h0q	81.00	6.10	F606W	30.0	04:57:48	2009-10-02
ibc601h2q	0.00	0.00	F606W	360.0	05:11:38	2009-10-02
ibc601h3q	0.00	81.59	F606W	360.0	06:07:31	2009-10-02
ibc601h5q	81.00	6.10	F606W	360.0	06:15:39	2009-10-02
ibc602urq	0.00	0.00	F502N	60.0	18:02:51	2010-03-25
ibc602usq	0.00	81.59	F502N	60.0	18:06:03	2010-03-25
ibc602uuq	81.00	6.10	F502N	60.0	18:20:25	2010-03-25
ibc602uvq	0.00	0.00	F502N	420.0	18:23:35	2010-03-25
ibc602uxq	0.00	81.59	F502N	420.0	18:32:43	2010-03-25
ibc602uzq	81.00	6.10	F502N	420.0	18:41:51	2010-03-25
ibc602v1q	0.00	0.00	F606W	30.0	18:51:24	2010-03-25
ibc602v3q	0.00	81.59	F606W	30.0	19:34:43	2010-03-25
ibc602v4q	81.00	6.10	F606W	30.0	19:37:25	2010-03-25
ibc602v6q	0.00	0.00	F606W	360.0	19:51:15	2010-03-25
ibc602v7q	0.00	81.59	F606W	360.0	19:59:23	2010-03-25
ibc602v9q	81.00	6.10	F606W	360.0	20:07:31	2010-03-25
ibc603zcq	0.00	0.00	F502N	60.0	06:23:21	2010-09-02
ibc603zdq	0.00	81.59	F502N	60.0	06:26:33	2010-09-02
ibc603zfq	81.00	6.10	F502N	60.0	06:40:55	2010-09-02
ibc603zgq	0.00	0.00	F502N	420.0	06:44:05	2010-09-02
ibc603ziq	0.00	81.59	F502N	420.0	06:53:13	2010-09-02
ibc603zkq	81.00	6.10	F502N	420.0	07:48:56	2010-09-02
ibc603zmq	0.00	0.00	F606W	30.0	07:58:29	2010-09-02